


Axial field induced spin response in Fe/hBN-based tunnel junctions

Aniekan Magnus Ukpong*

Theoretical and Computational Condensed Matter and Materials Physics Group, School of Chemistry and Physics, College of Agriculture, Engineering, and Science, University of KwaZulu-Natal, 1 King Edward Avenue, Scottsville 3201, Pietermaritzburg, South Africa (Received 8 March 2019; revised manuscript received 15 May 2019; published 18 July 2019)

First-principles calculations of spin transmission and perpendicular magnetic anisotropy in artificially stacked Fe(110)/hBN/metal heterostructures have been employed to study the dynamical response of tunnel junctions to applied axial fields. By projecting the effective electric-field gradient densities and magnetic shielding constants across constitutive atomic layers in the scatter region of the device, an unusual site-dependent spin response is unraveled at the Fe/hBN and hBN/metal heterobilayer interfaces. Analysis of the Fermi-level topology reveals an exotic electronic phase characterized by electric-field induced spin flip relative to the ferromagnetic ground state. The calculations reveal unique signatures in the spin transport phase and dynamical effects are observed as field tunable perpendicular magnetic anisotropy. In particular, magnetization alignment preferences are observed in the spin transmission, electric-field gradient localization, and a vanishing magnetic shielding at finite electric fields. Results show that V-capped stacks have a relatively superior perpendicular magnetic anisotropy suggesting that the atomic species of the free layer plays a dominant role in spin-based information storage using Fe(110)/hBN/M stacks.

DOI: [10.1103/PhysRevB.100.035424](https://doi.org/10.1103/PhysRevB.100.035424)**I. INTRODUCTION**

Perpendicular magnetic tunnel junctions (pMTJs) are central to nonvolatile random access memory elements. Typically, a large perpendicular magnetic anisotropy (PMA) is required to achieve thermal stability. There are two main challenges to the integration of pMTJs in spintronics: precise atomic-level control of the orientation of spin, and an improved thermal stability. For instance, in the technologically important CoFeB/MgO-based pMTJs, a significant issue is the low thermal stability that arises due to rapid degradation in PMA at $T > 300$ °C [1]. Despite concerted research on MTJs, the most widely used tunnel barrier materials are still MgO and Al₂O₃. The main problem with metal oxides is that they present a nonuniform structure, which gives rise to incoherent topographies over their thicknesses. This is because their local structure contains a diverse array of structural defects when their dimension is reduced from bulk to two-dimensional (2D) form. All these factors have a negative influence on the device performance. As a result, it is intrinsically difficult to control these oxides at the monolayer scale desirable for 2D spintronics. Recently, the characterization of spin valves based on pMTJ architectures that incorporate 2D materials has attracted considerable interest [2–5].

The use of 2D materials in pMTJs is appealing for spintronics because of their structural uniformity, thermodynamic stability, and unique potential for precise atomic-level control of the tunneling spin current. This is because the local atomic structure in 2D materials is highly homogeneous over their thickness. Their structural uniformity means that their interfaces with other component layers of the pMTJ are atomically thin. This ensures minimization of spin scattering from defect

states. In addition, the high oxidation and thermal stabilities of monolayer hBN endow it with superior chemical inertness. This makes the vertical transport of coherent spin currents by tunneling through the 2D materials in pMTJs robust to perturbations unlike in the prototypical MTJs, which are based on three-dimensional (3D) materials. Their fabrication is done through layer-by-layer stacking of physically transferred thin films of similar or dissimilar materials stacked into a multilayer heterostructure. Thus, insight into the robustness of the spin signatures to axial fields in artificially assembled electronic materials is central to achieving spintronics based on 2D materials.

In strong magnetic fields, transport experiments usually show a variety of fascinating quantum phenomena, which originate from the atomic-scale structure. However, such structural information is the most inaccessible to macroscopic magnetotransport experiments [6]. To link the local structure with signatures derived from spin transport properties, advanced experimental methods and probe techniques are required. It is therefore not unusual to ask the following: how do such signatures in artificially stacked Fe/hBN/metal-based pMTJs respond to electric and magnetic fields in typical conditions that mimic memory elements? Such insights are important in spintronics since pMTJs require a large magnetocrystalline anisotropy energy (MAE) in order to preserve data stored in the magnetic state of the information vector [7]. Electric-field dependent PMA is analogous to the voltage-controlled magnetocrystalline anisotropy (VCMA) that determines information-storing capacity. As MAE is an interplay of spin-orbit coupling (SOC), ligand field effect, and broken spatial inversion and time-reversal symmetries, it is important to understand how magnetic properties are controlled by the atomic interface [8,9] and how to tune spin currents using axial fields [10].

*ukponga@ukzn.ac.za

Here, the dynamical effects of external axial fields are investigated in scatter regions of MTJs modeled as Fe(110)/hBN/ M multilayers. It is demonstrated that field reversible tuning of the PMA occurs in Fe(110)/hBN-based pMTJs. A first-order polarization is obtained as enhanced spin transmission at preferred spin alignments, electric-field gradient (EFG) localizations, and a vanishing magnetic shielding. An unusual site-dependent response is observed in the spin-pumping regime of the Fe/hBN and hBN/Co heterobilayer interfaces. Analysis of the Fermi-level topology reveals an exotic electronic phase characterized by electric-field induced spin flip relative to the ferromagnetic (FM) ground state. These calculations reveal unique signatures in the spin transport phase, in addition to the dynamical effects, which are observed as field-tunable PMA. The computed responses to applied fields offer unique insights to field induced changes in the spin transport from the trivial metallic to exotic phases in the regime of high electric fields.

This paper is organized as follows. In Sec. II, the theoretical framework employed here to calculate the electronic structure in the presence of an axial field is provided. Computational details are also provided for the protocols used to generate pMTJ models in first-principles calculations. The latter includes structure optimization strategies that describe artificial multilayers fabricated as layer-by-layer stacking of dissimilar thin films. In Sec. III, the zero-field properties and spin transport signatures in Co-, V-, and Ni-capped heterostructures are presented. The response of tunneling spin current to external axial fields is also analyzed in Sec. III with respect to simulated NMR parameters and the topology of the Fermi surface (FS). Finally, conclusions are drawn in Sec. IV.

II. THEORETICAL AND COMPUTATIONAL METHODS

The pMTJs investigated herein are heterostructure multilayers modeled as van der Waals stacks [11]. These are obtained as vertically stacked multilayers of two dissimilar FM materials separated by the monolayer hexagonal boron nitride (hBN) tunnel region. Due to its wide band gap and chemical inertness, monolayer hBN has been used in pMTJs as the tunnel barrier [2–5]. The monolayer hBN tunnel region has the unique advantage of eliminating resonant tunneling in vertically transported spin current [12]. Recently, spin-injection devices have been fabricated based on Fe/hBN/Co pMTJs using a direct CVD step on the top of the Fe to grow the monolayer hBN sheet [3,4]. By contrast, Zollner *et al.* [13] studied the lattice-matched graphene/hBN/Co heterostructure computationally for one hBN layer. Because hBN is a non-magnetic semiconductor (NS), the pMTJs are asymmetric. Its FM/NS/FM architecture represents a scatter region of Fe(110)/hBN/ M stacks attached to infinite Fe and M leads, where $M = \text{Ni}(111)$, $\text{Co}(111)$, or $\text{V}(111)$.

Equilibrium lattice constants obtained from calculations with the PW91 functional are converged to $a(\text{Fe}) = 2.857 \text{ \AA}$ for bcc Fe, $a(\text{Co}) = 2.502 \text{ \AA}$ for hcp Co, $a(\text{V}) = 3.031 \text{ \AA}$ for bcc V, $a(\text{Ni}) = 3.52 \text{ \AA}$ for fcc Ni, and $a(\text{hBN}) = 2.51 \text{ \AA}$. Each isolated component of the stack is modeled as an infinite periodic slab in the xy plane with four atomic layers. Each stack is then capped with different metallic (M) free layers, i.e., Co, Ni, or V, to form van der Waals multilayer het-

erostructure in each case. Thus, although the lattice constant of the Co layer (2.502 \AA) matches well with the 2.51-\AA lattice constant of the monolayer hBN tunnel barrier, the comparatively larger lattice constant of the Fe layer (2.857 \AA) means that structural commensurability requires a very large supercell if the hBN/Co heterobilayer is stacked vertically on the Fe(110) substrate via vdW interaction. This inadvertently results in a very large number of atoms in the unit cell, which makes it impractical to implement density functional theory (DFT) calculations within periodic boundary conditions.

As a compromise, effective average lattice constants, $a = 4.26 \text{ \AA}$ and $b = 3.00 \text{ \AA}$, are fixed for the stacks to keep the unit cell as small as possible. The component layers are stacked vertically into a multilayer heterostructure inside the atomic simulation environment (ASE) [14]. The ASE is an open source PYTHON library for working with atoms. To generate stacks in ASE, the alignment and relative orientation of a transferred layer are adjusted to fit above the underlying surface. Importantly, lattice-matching restrictions are completely lifted since the atoms of the transferred layers are physically constrained within their layer, and thus not free to locate any particularly favorable adsorption site(s). This protocol ensures that the scatter region, though strained, maintains its periodicity along the xy plane. The positions of Fe and M atoms within the outermost atomic plane of the two heterobilayer interfaces are always fixed at their bulk positions in metallic leads, leaving the heterobilayer interfaces to absorb the lattice mismatch strain during position relaxation. The only restriction imposed on the stack models is that relaxation of atomic positions must compensate for any existing mismatch strain across constituent heterolayer interfaces without any local reconstructions of the interfacial structure and (or) puckering of the hBN monolayer. A $12 \times 12 \times 1$ k -point mesh was used for the position-relaxation calculations, after inserting a vacuum region of 25 \AA to isolate periodic cells from spurious image interactions. Total energy of the stacks was converged with respect to k -mesh size. The adhesion energy was also converged with respect to the thickness of the Fe(110) and the M -capping layer slabs.

The calculations were performed using the nonempirical spin-density form of the van der Waals density (svdW-DF2) functional [15] as implemented in the plane-wave self-consistent field code of QUANTUM ESPRESSO (QE) [16]. The svdW-DF2 functional denotes the spin-polarized form of the second version of the Dion *et al.* model [17] of the van der Waals density functional (vdW-DF2) originally proposed by Lee *et al.* [18]. The exchange-correlation potential is treated in the generalized gradient approximation since the vdW-DF2 functional uses the refined version of the Perdew and Wang (PW86) functional as the gradient correction on exchange [19,20], in combination with a nonlocal correction for dispersive interactions, for which $Z_{ab} = -1.887$ [21]. Cutoff limits of 70 and 800 Ry were used for the kinetic-energy and charge density expansions in the plane-wave basis. The Brillouin zone was sampled with a $12 \times 12 \times 1$ Monkhorst-Pack k -point grid [22]. However, the much denser mesh of $30 \times 30 \times 1$ k points is used to calculate the Fermi surface. Electron states are treated as spinors, with double group symmetry, and populated using Marzari-Vanderbilt cold smearing with width of 0.0074 Ry [23]. Electronic energy was converged

to within 10^{-6} Ry. In the zero-field limit, the interaction between valence electrons and ion cores is described using PAW potentials [24]. Atomic positions are relaxed until Hellman-Feynman forces on each atom are less than 10^{-3} eV/Å.

Spin carries information about interactions such as MAE, spin orbit torque, exchange splitting, etc. Spin transmission was calculated at variable external electric and magnetic field using the Landauer-Büttiker formalism [25]. The force theorem approach [26–28] was used to calculate MAE. The procedure is to first perform a self-consistent collinear magnetization calculation without SOC for the structure relaxation. This relaxed structure is then used as the input charge density for the second noncollinear magnetization calculation. SOC is included self-consistently as a first-order perturbation of the spin state using relativistic PAW potentials. SOC lifts Kramers degeneracies by splitting electron states that are degenerate when it is not included. However, further relaxation in structure due to the inclusion of SOC is ignored. Two high-symmetry directions of alignment of magnetization are used in order to determine MAE. Since MAE depends on the choice of spin quantization axis, ambiguity was avoided by using the [100] axis of the pMTJ stack for *in-plane* and *out-of-plane* magnetization. With SOC included, MAE is obtained as the energy difference between two noncollinear spin configurations the magnetizations of which are aligned along *easy* and *hard* axes. Positive MAE therefore implies out-of-plane easy axis, denoted herein as the PMA [29].

Consider that the ground state is determined at DFT level using the effective screening medium technique [30] by applying the vacuum-slab-vacuum boundary conditions to the unit cell. Recently, this approach has been used to describe graphene-based vertical field-effect tunneling transistors [31] and gated two-dimensional heterostructures [32]. Gauge-including projector augmented wave (GIPAW) potentials [33] are subsequently used to account for ionic interactions in external electric or magnetic field. Correct potentials are recovered in the stack from the GIPAW calculations in the absence of the external gauge field. Therefore, it is relevant to determine whether the applied external field is not extremely low or high for the spin response in the stacks. Herein, the local potential difference at zero field (ΔV) is used as the descriptor of the electronic structure. Variations in ΔV are used to investigate the response of the ground-state electron-spin density to different intensities of the applied electric field. In addition, other physical observables of the spin response such as EFG tensors, the nuclear quadrupolar coupling constant (C_Q), and the quadrupolar asymmetry parameter (η_Q) were also computed using the GIPAW code of the QE package [16].

In order to validate this approach of using ΔV as the estimator of the field effect on the electronic structure, the polarity of the interfaces is studied at zero field to explore how the charge density and local potential vary across the heterostructure. As translational periodicity is maintained only along the xy plane, the planar charge density ρ and planar potential V (each is denoted by the scalar function Φ) are obtained as averages along atomic planes parallel to the z axis of the scatter region, where

$$\tilde{\Phi}(z) = \frac{1}{L} \int \Phi(x, y) dy. \quad (1)$$

Bulk effects are eliminated to correctly describe the response of the scatter region by taking the average of observables. Thus, macroscopic averages of each plane-averaged quantity $\tilde{\Phi}(z)$ are determined over the length c of the unit cell [34]. Planar charge density and total potential are then calculated, as convoluted line averages $\tilde{\tilde{\Phi}}(z)$ along the z axis of the stack using the relation

$$\tilde{\tilde{\Phi}}(z) = \frac{1}{c} \int_0^z \tilde{\Phi}(z') dz'. \quad (2)$$

III. RESULTS AND DISCUSSION

A. Zero-field properties

1. Local structure

The setup of multilayer stacks and position optimization mimics the actual fabrication of spin valve devices because the layer-by-layer stacking of physically transferred films is not equivalent to nucleation of atomic species on a substrate from the gas phase. Thus, it is both implausible and counterintuitive for individual atoms in physically transferred thin films of a heterogeneous multilayer stack to adopt *a priori* favorable nucleation geometries expected for adatoms nucleating on the substrate from the gas phase. As a result, the distributions of atomic positions, interlayer distances, and interface geometries in the stack are not expected to be symmetric—even in symmetric pMTJs. Nevertheless, maintaining the structural integrity of the Fe/hBN and hBN/ M interfaces and controlling their spin transport properties with external axial fields are most desirable.

Figures 1(a)–1(c) show the scatter region after position relaxation, and Fig. 1(d) shows the schematic of a typical device in measurement configuration. Notwithstanding the nature of the capping layer, M , the hBN monolayer is atomically flat. This is a crucial requirement in fabricating spin valves through layer-by-layer stacking of physically transferred layers. Interlayer separations between Fe(110)/hBN and hBN/ M heterobilayer interfaces are sensitive to the capping metal. Between Fe(110) substrate and monolayer hBN, the separation distance is 3.09 Å (Co), 3.31 Å (Ni), and 2.86 Å (V), in each case. Between hBN and the capping slab, by contrast, the distance is 3.36 Å (Co), 3.56 Å (Ni), and 4.05 Å (V), respectively. Atomic positions and interlayer distances show an asymmetric distribution depending on M . Because the spin tunneling event can either occur at the physisorption or chemisorption interface, wave-function overlaps must occur at Fe/BN and hBN/ M interfaces [35]. Figure 1 also reveals atomically thin physisorption interfaces expected when monolayer hBN is incorporated in spin valves [2,3]. In physisorption, dispersive forces (or van der Waals interactions) couple the component materials together to preserve the π -band structure of the hBN monolayer, as opposed to the promotion of pd hybridization by orbital mixing, as expected in chemisorption [36].

The distribution of first-nearest-neighbor distances suggests a relaxation of strain across the interfaces. Aside the persistent lattice mismatch, first-nearest-neighbor B-N distance is 1.42 Å in all directions within the Fe(110)/hBN/Co(111) stack. This is shorter than the 1.45 Å obtained in the free-standing pristine hBN monolayer, or the experimental B-N bond length of 1.44 Å in hBN [37,38]. Nevertheless,

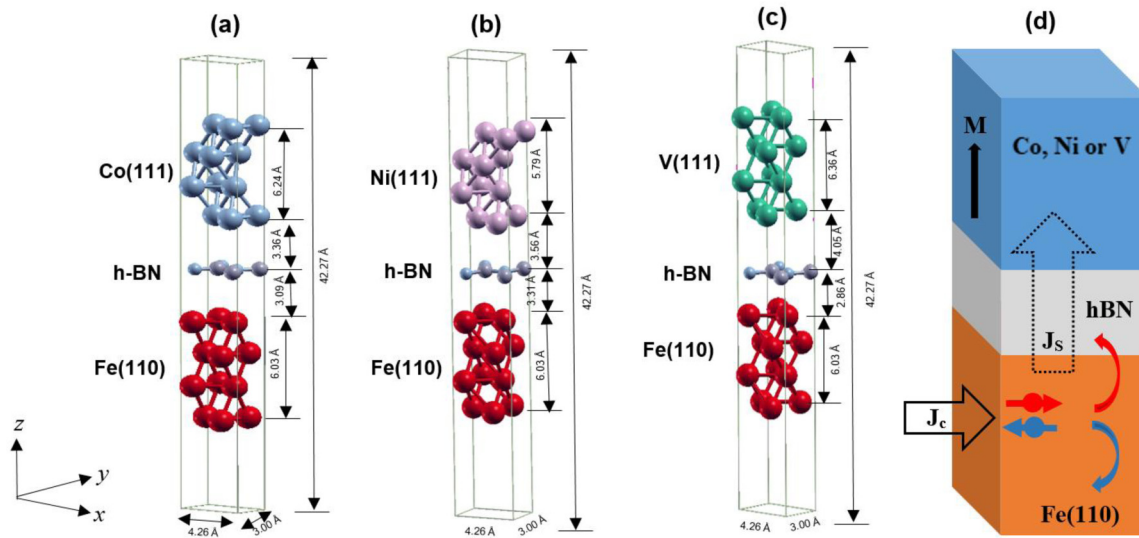


FIG. 1. Interlayer distances and local structure in the unit cell of (a) Fe(110)/hBN/Co(111), (b) Fe(110)/hBN/Ni(111), and (c) Fe(110)/hBN/V(111) multilayers after position relaxation. (d) Schematic of the pMTJ in measurement geometry, where \mathbf{M} is the magnetization vector and \mathbf{J}_s and \mathbf{J}_c are the injected spin-polarized current density and nonpolarized current density, respectively.

the calculated B-N bond lengths are consistent with results of other calculations [39–41]. By contrast, the corresponding B-N interatomic distances are direction dependent in Fe(110)/hBN/Ni(111) and Fe(110)/hBN/V(111) stacks. In each case, the B-N bond lengths are 1.43 Å (in plane) and 1.65 Å (out of plane, i.e., the z axis of the stack). The Fe-Fe (and M - M) near-neighbor distances are also sensitive to the capping layer. The largest change in Fe-Fe bond length is along the z axis of the stack for $M = \text{Co}$. Nevertheless, interface strain modifies the local bonding structure and causes uneven distribution of charges and local magnetic moments.

Thus, the residual lattice mismatch strain is carried mainly in the intralayer bond distances and through the asymmetric distribution of interlayer distances during the position relaxation calculations (see Fig. 1). Interlayer distances that are either shorter or longer than the corresponding equilibrium interatomic distances imply that the layer is under either strong chemisorption or strong biaxial strain. Compensating for strain at constituent heterolayer interfaces without local reconstruction of the interfacial structure and puckering of the hBN monolayer means that the layers must remain coupled in the stack. Thus, to characterize the stability of the stacks, the convergence of the adhesion energy was also tested for different thicknesses of the Fe(110) layer and M -capping layer. In the four-monolayer slab model, the adhesion energy converges to 0.388 J m^{-2} (Co capped), 0.792 J m^{-2} (Ni capped), and 2.56 J m^{-2} (V capped), respectively. Clearly, the adhesion energy decreases as more atomic monolayers are incorporated in the slab models for all capping M species. Overall, the adhesion energies are positive irrespective of the species of the M -capping layer, indicating that the stacks are stable. More details of the total energy of the stacks, and their component materials, as well as adhesion energy convergence with respect to k -mesh size, can be found in the Supplemental Material [42].

For all components of the stacks, our calculations also give converged structural parameters in agreement with experiments and results of other calculations of the hBN monolayer [38,43–45], Co(111) [44,45], Ni(111) [44–46], V(111) [47–49], and Fe(110) [45,50–53] surfaces. The calculated B-N bond length of 1.45 Å for free-standing pristine hBN monolayer also agrees with other calculations of monolayer hBN [39–41,54,55]. In addition, the predicted bandgap of 5.95 eV is consistent with the ~ 6 eV [56,57] obtained in experiments. Structural properties of the metal components of stacks show that Ni, V, and Co slabs each retains the expected fcc (111) local structure after position relaxation. The predicted local structure of the Fe(110) surface slab is an ordered bcc structure, which is consistent with other recent calculations that give low surface energies for the Fe(110) facet of bcc Fe at 0 K [52,58], and at finite temperatures up to 1850 K [59]. In free-standing metallic slab components of the stacks, the distribution of magnetic moments at atomic sites as a function of the depth from the surface agrees well with the trends from tight-binding generalized gradient approximation model calculations [60]. Each of the coupled multilayer stack system forms an asymmetric pMTJ akin to the spin filter tunnel junctions (SFTJs) fabricated in [3,4,61–69] through layer-by-layer stacking of physically-transferred thin film components, although symmetric pMTJs can also be fabricated using this method. Nevertheless, it is crucial to note that in spite of the presence of a large lattice mismatch strain in lattice-mismatched substrates of the device architecture, spin-injection devices are now routinely fabricated using a direct CVD step on the top of “specially-prepared” or “patterned” surfaces in order to grow the monolayer hBN sheet directly [70–72].

2. Local potentials

Table I shows the localized charge (q) and magnetic moment (m) at atomic sites in Fe(110)/hBN/ M stacks. The

TABLE I. Charge (e) and magnetic moment (m) per atomic site in Fe(110)/hBN/ M stacks.

Site	Fe(110)/hBN/Co(111)		Fe(110)/hBN/Ni(111)		Fe(110)/hBN/V(111)	
	$q(e)$	$m(\mu_B)$	$q(e)$	$m(\mu_B)$	$q(e)$	$m(\mu_B)$
Fe8	12.34	1.79	14.40	2.55	14.40	2.54
Fe7	8.96	1.28	14.34	2.69	14.35	2.69
Fe6	12.35	1.79	14.40	2.55	14.40	2.54
Fe5	8.92	1.27	14.34	2.69	14.35	2.69
Fe4	13.45	1.99	14.40	2.54	14.40	2.51
Fe3	13.89	2.19	14.35	2.68	14.33	2.66
Fe2	13.44	1.99	14.40	2.54	14.40	2.51
Fe1	13.90	2.19	14.35	2.68	14.33	2.66
B1	0.85	-0.0001	0.74	-0.001	0.51	-0.003
N1	2.74	0.001	2.71	0.004	1.81	0.002
B2	0.85	-0.0001	0.74	-0.001	0.51	-0.003
N2	2.74	0.001	2.71	0.004	1.82	0.002
M1	6.81	1.64	8.54	0.68	9.05	-0.002
M2	7.04	1.62	8.60	0.68	10.83	0.002
M3	6.81	1.64	8.54	0.67	9.04	-0.002
M4	7.04	1.61	8.60	0.68	10.83	0.002
M5	5.37	1.11	8.53	0.70	7.90	0.002
M6	6.38	1.45	8.60	0.69	10.58	-0.0004
M7	5.36	1.11	8.54	0.70	7.90	0.002
M8	6.38	1.45	8.60	0.69	10.58	-0.0004

pair of atoms Fe1-Fe2 and $M1$ - $M2$ forms the heterobilayer interface with monolayer hBN in each case. Thus, atoms Fe7-Fe8 and $M7$ - $M8$ are furthest from the interface and fixed at their bulk positions during position optimization. Near the hBN layer, significant charge accumulation occurs. Crucially, the interfacial Fe atoms in Fe(110)/hBN/Ni(111) and Fe(110)/hBN/V(111) stacks do not exhibit the same trends in charge and magnetic moment localization densities. The charge on atoms Fe1 and Fe2, i.e., within the first atomic layer of Fe(110), is $13.90e$ and $13.44e$, respectively. A similar magnitude of charge is also obtained on Fe3 and Fe4 atoms of the second atomic layer in the Fe(110) slab. The third and fourth layers behave as bulk Fe and retain unequal charges.

These show a significant accumulation of charges on the interfacial Fe and M species. Each topmost atomic layer of the

heterobilayer contains an equal number of B and N atoms, but with unequal charges localized on atoms of the ferromagnet. The number of valence electrons in Fe is 8, but all M species have different valence electrons, i.e., Co(4), V(5), and Ni(10). Apart from B and N, all other atoms in the stack have the same valency of +2 in metallic bonds. Consider that Fe1-Fe2 and $M1$ - $M2$ pairs form two heterobilayer interfaces with an equal number of B and N atoms in the barrier layer. The differences in charge buildup between Fe and M species manifests as a finite potential difference (ΔV) across heterobilayer interfaces. These zero-electric-field effects are thus attributable to the increased magnetic moment around Fe atoms at the interface, although PMA is sensitive to the number of layers in the slabs.

Figure 2 shows plane-averaged electronic pseudo charge density and the corresponding total local potential in

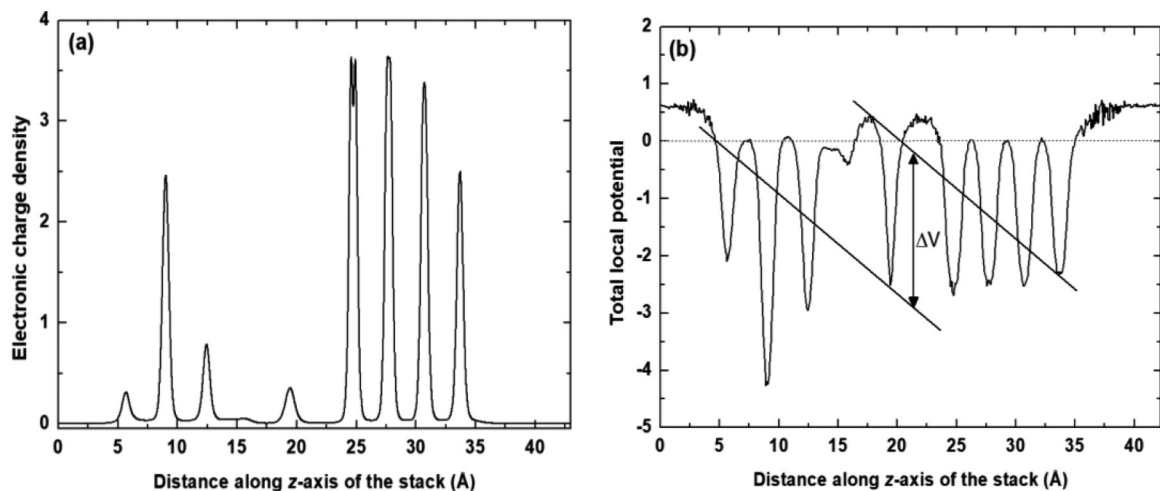


FIG. 2. Planar average charge density (a) and total local potential (b) at zero electric field normalized along the c direction of the unit cell ($c = 42.27 \text{ \AA}$).

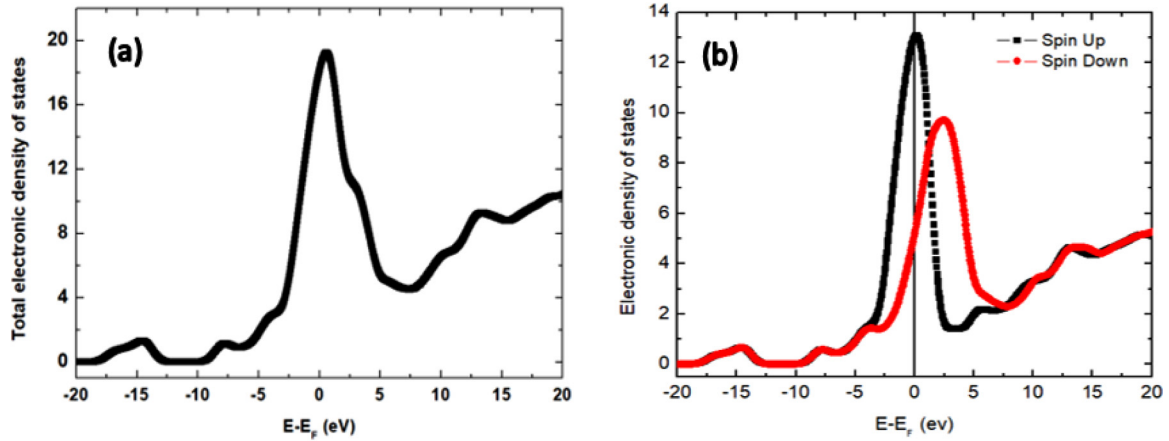


FIG. 3. (a) Electronic structure of the Fe(110)/hBN/Co(111) multilayer showing the total DOS. (b) Spin-resolved DOS showing Hanlé-type spin splitting around the Fermi level.

Fe(110)/hBN/Co(111) at zero applied field. Outside the physical region of the multilayer structure, the charge density is zero. The vanishing charge densities in the extremal regions of Fig. 3(a) correspond with the vacuum region of Fig. 1. The charge density is distorted and asymmetrically distributed over the multilayer heterostructure. There are distinct charge density peaks, wherein Fe slab planes of the Fe(110)/hBN interface exhibit lower charge density distributions relative to the Co atomic planes of the hBN/Co interface. In the physical region of the stack, the unequal charge density profile suggests a buildup of electron density on the four atomic layers of Co relative to the hBN monolayer and the four atomic layers of the Fe. The charge buildup across the two interfaces is illustrated in Fig. 2(b). Discontinuity in the local potential across Fe(110)/hBN and hBN/Co(111) interfaces manifests as finite difference in the local potential (ΔV). The critical field $\Delta V = 2.58$ V is obtained at zero external electric field. The dipolar effect of ΔV is shown in Fig. 2(b). It is assumed that the electronic density remains in the linear response regime of the applied electric field, so that ΔV can serve as the estimator of the response of the electronic structure to applied external fields. Hence, the evolution of ΔV with changes in the intensity of the electric field is probed to characterize the electronic spin transport phase, especially at high electric fields.

3. Electronic structure

Figure 3 shows the electronic density of states (DOS) in Fe(110)/hBN/Co(111). It can be concluded that the majority-spin dominates at the Fermi level ($E_F = 0.0$ eV). The spin-polarized electronic DOS shows that electron states in the multilayer stack are characterized by split states around the E_F , which partitions into distinct spin-up and spin-down DOSs. The Hanlé-like effect is observable as a reduction in the spin-down DOS in Fig. 3(b). The DOS splits asymmetrically in both spin channels, showing that spin occupancy of the electron state is inherently susceptible to the perturbing effects of externally applied fields. In Fig. 3(a), the shoulder on the main peak at 2.5 eV suggests that raising E_F to +2.5 eV will favor spin-down carrier transport because minority carriers dominate at the now tuned E_F .

Figure 4 shows the distribution of spin-polarized electronic energies, and the corresponding 2D Fermi surface for spin-up (top panels) and spin-down (bottom panels) channels. The unshifted E_F is 2.34 eV. The energies are projected on pairs of wave-vector points (k_x, k_y) in the 2D irreducible Brillouin zone. The contour lines [Figs. 2(a) and 2(c)] show that electronic energies are characterized by nonuniform dispersion. The dependence of energies on wave vector in both spin channels is a combination of both strong and weak dispersions, in agreement with structural trends in interlayer couplings (see Fig. 1). The energy distributions show localized regions of high and low energies as similar regions of the Brillouin zone. Extremal points in the distribution correspond to domains of low (or high) energies wherein small pockets form in the FS. The energy distributions in Figs. 4(a) and 4(c) are similar insofar as the position of the localized regions of high and low energies on the contour maps are concerned.

Figures 4(b) and 4(d) show underlying features in the FS topology of the spin-up and spin-down channels in the zero-field limit. Clearly, the spin transmission coefficients at E_F are sensitive to the field induced response of the underlying electronic structure. The FS is gapped out at the zone center, edges, and corners of the spin-up channel [Fig. 4(b)]. The Fermi arcs are unevenly spaced out in the spin-up channel [see Fig. 4(b)]. Four Fermi arcs merge at points 1 and 2, but unequal gaps develop at points 3, 4, 5, and 6. In Fig. 4(b), we find that the closely spaced pair of Fermi arcs forms closed loops along the X - M direction at crossing points 1 and 2. Figure 4(d) shows that the topology is significantly less gapped at Γ and M in the spin-down channel. Around the zone center, Brillouin-zone points merge to form distinct closed loops. These manifest as four circular and two oblate loops, and two large triangular loops along the Γ - X direction.

The closed loops also manifest as FS nesting at the zone edges (X points) in both spin channels. These signatures are similar to the topological node line transport states predicted in 3D graphene [73], CaTe [74], and ZrSiTe [75]. There are several distorted node lines in the X - M direction. Because the Fermi arc at point X in the spin-down channel is not closed, transport of spin-down carriers is susceptible to spurious quantum oscillations. Such oscillations do not appear in the

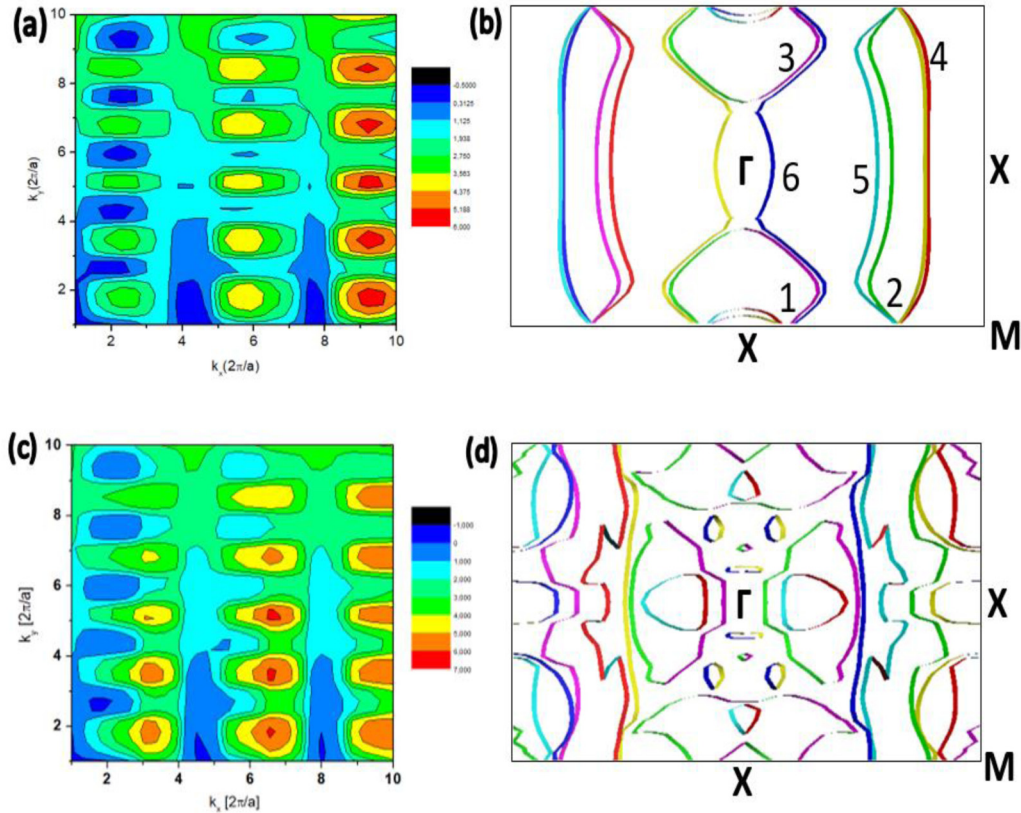


FIG. 4. Distribution of spin-resolved electronic energies around the Fermi surface and its topology in the spin-up (top panels) and spin-down (bottom panels) channels.

zero-field spin transmission spectra due to the absence of quantum-well states in monolayer tunnel barriers [76]. The modulation of the Fermi surface suggests the presence of an exotic transport phase at sufficiently high applied electric fields and exhibits different properties in the zone-center carrier transport character of both spins' channels. Several nodal lines exist in the spin-down Fermi-surface topology around the Γ point. Thus, even with atomically thin interfaces, the susceptibility of spin magnetotransport in the Fe(110)/hBN/Co(111) multilayer to electric-field dependent oscillations introduces phase shifts in the tunneling spin current.

4. Spin tunneling

Figure 5 shows the spin transmission coefficients at zero bias for parallel and antiparallel spin alignments. In each case, a dominant peak is seen around the top of the valence band near the Fermi level (E_F). This suggests the possibility of a preferential transmission of the spin-up (or spin-down) channel when the spin alignment is in parallel (or antiparallel) configuration. It is shown in Sec. III B 4 that, irrespective of the spin alignment, the spin-up carrier transmission coefficient is not always dominant at E_F . Instead, we find strong sensitivity to the electric field, through which coherent

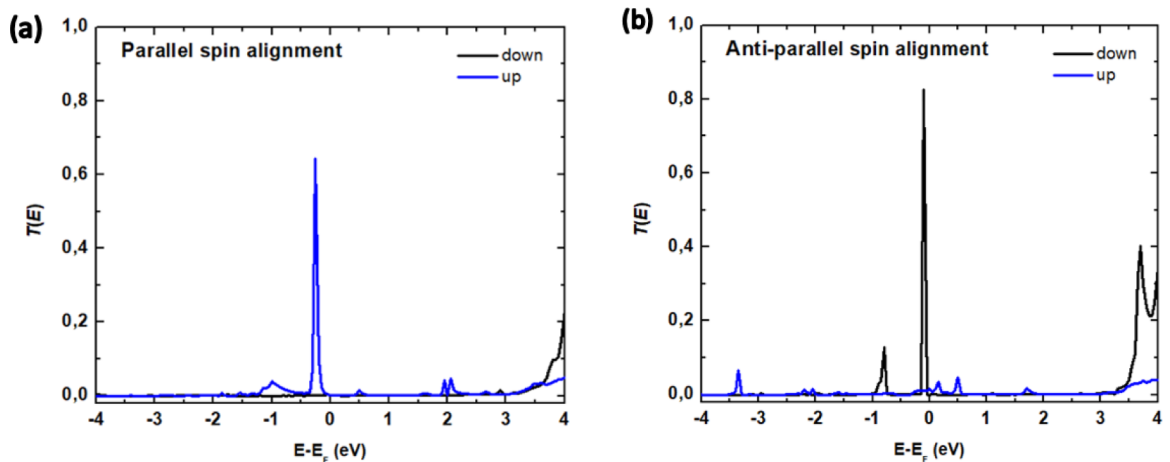


FIG. 5. Spin transmission probability at zero bias in parallel (a) and antiparallel (b) alignments.

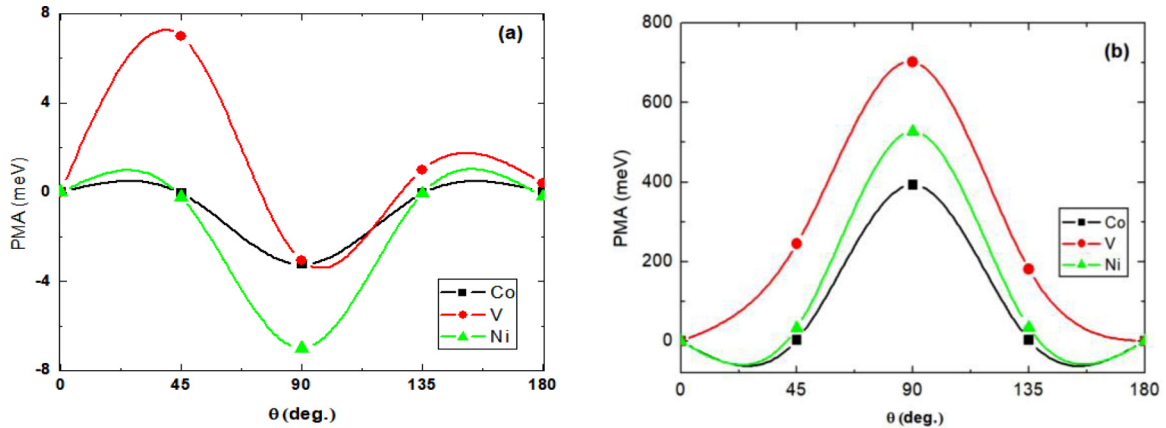


FIG. 6. Zero-field limit of the PMA in Fe(110)/hBN/ M stacks when the ferromagnetic electrodes are modeled with two atomic layers (a) and with four atomic layers (b).

transfer of magnetization is realized. The zero-field spin conductivity $G(E_F)$ is obtained from the transmission probabilities as $G(E_F) = G_0[T_\uparrow(E_F) + T_\downarrow(E_F)]$, where $G_0 = e^2/\hbar$ is the conductance quantum. Our results give $T_\uparrow(E_F) = 0.41$ and $T_\downarrow(E_F) = 0.20$, where $G(E_F)$ is $0.61 G_0$.

In parallel (or antiparallel) configuration, spin-down (or spin-up) conductance vanishes—even at high electronic energies. Parallel (or antiparallel) spin alignment with respect to the quantization axis clearly transmits up (or down) spin. The efficiency of the spin inversion at zero-bias tunneling determines the tunneling magnetoresistance (TMR), i.e., the change in resistance of the pMTJ when the alignment of magnetization in the two ferromagnetic layers is changed. In DFT calculations, $\text{TMR} = 100\% \times (G_{\uparrow\uparrow} - G_{\uparrow\downarrow})/G_{\uparrow\downarrow}$ [77]. In the spin filter approximation, calculation of TMR reduces to the evaluation of $T_{\uparrow\uparrow}(E_F)/T_{\uparrow\downarrow}(E_F)$, where $T_{\uparrow\uparrow}(E_F)$ and $T_{\uparrow\downarrow}(E_F)$ are the spin transmission coefficients for parallel ($\uparrow\uparrow$) and antiparallel ($\uparrow\downarrow$) alignments [78]. With $T_{\uparrow\uparrow}(E_F) = 0.18651$ and $T_{\uparrow\downarrow}(E_F) = 0.01207$, these *ab initio* calculations give $T_{\uparrow\uparrow}(E_F)/T_{\uparrow\downarrow}(E_F) = 15.45$. The spin polarization $P(E_F) = 87.84\%$ is obtained using $P(E_F) = \{[G_\uparrow(E_F) - G_\downarrow(E_F)]/[G_\uparrow(E_F) + G_\downarrow(E_F)]\}$, with a corresponding bias-tunable TMR of 4.74% [2,5].

Figure 6 shows magnetic field effects on the zero-electric-field limit of the PMA when both Fe and M electrodes are modeled with two atomic layers [Fig. 6(a)] and with four atomic layers [Fig. 6(b)]. In each case, the rotation angle $\theta = 0^\circ, 45^\circ, 90^\circ, 135^\circ$, and 180° corresponds to the saturation magnetization $M_s = +1, +0.5, 0, -0.5$, and -1.0 , which is induced by the magnetic field. Clearly, magnetization increases as the intensity of the applied magnetic field is increased. With PMA at $\theta = 0^\circ$ set as reference state, 100% spin-up configuration corresponds to the parallel alignment ($\uparrow\uparrow$) induced by the applied magnetic field. Control of θ with the external magnetic field allows the simultaneous control of M_s to reveal dynamical field effects.

PMA is sensitive to the number of atomic layers used to model the electrodes. The largest PMA is obtained at $\theta = 90^\circ$ (and lowest at $\theta = 0^\circ$) notwithstanding the nature of M . For $M = V$, the peak PMA increases by 100-fold when four atomic layers are used relative to two layers. In the two-atomic-layer model, rapid oscillations are observed in the

PMA as θ changes [Fig. 6(a)]. Using four atomic layers, a comparatively smaller PMA is observed for Co relative to V or Ni. For instance, extremal PMA values are 702 meV (V) and 527 meV (Ni) at 90° compared to 393 meV (Co) at the same magnetic field intensity or spin orientation. Figure 7(b) clearly shows the sensitivity of the magnetic field dependent switching of the PMA in Fe(110)/hBN/ M stacks on the nature of the M species.

B. Finite-field effects

Consider that applied fields lift the constraint, i.e., $E(k) = E(-k)$, imposed on electron states by time-reversal symmetry. It is observed [Figs. 6(a) and 6(b)] that reversing the orientation of the magnetic field does not leave the spin eigenstates invariant. For instance, $\text{PMA}(\theta = 45^\circ) \neq \text{PMA}(\theta = 135^\circ)$, and small differences also exist in PMA when spins are aligned along $\theta = 0^\circ$ and 90° . Moreover, the local structure lacks spatial inversion symmetry. Hence, the change in the zero-field PMA is attributable to the absence of a *global* crystal structure, on which the PMA in the stack should depend. Thus, focus is now on the responses of the local structure and magnetic properties in Fe(110)/hBN/Co(111) to the applied electric field. Hereunder, the spin decoherence obtained at high electric fields manifests as a switch in the net magnetization density.

1. Magnetization density

Table II shows the effects of electric field on magnetization in the Fe(110)/hBN/Co(111) stack. Changes in magnetic properties due to the applied field are characterized in terms of configurational differences (Δ) between two collinearly magnetized configurations. Absolute magnetization (M_A) and total magnetization (M_T) are maximal in the zero-field limit, and vanishingly small (or even zero) in the collinear nonmagnetic configuration under the influence of the applied electric field. A progressive decrease is observed in both M_T and M_A with increasing electric-field intensity. M_T and M_A are also sensitive to the capping layer. For instance, $M_T = 1.55$ and $M_A = 1.64$ (in μ_B/atom) in Fe(110)/hBN/Co(111). These are far higher than $M_T = 1.31$ and $M_A = 1.40$ and $M_T = 1.04$ and $M_A = 1.09$ (in μ_B/atom)

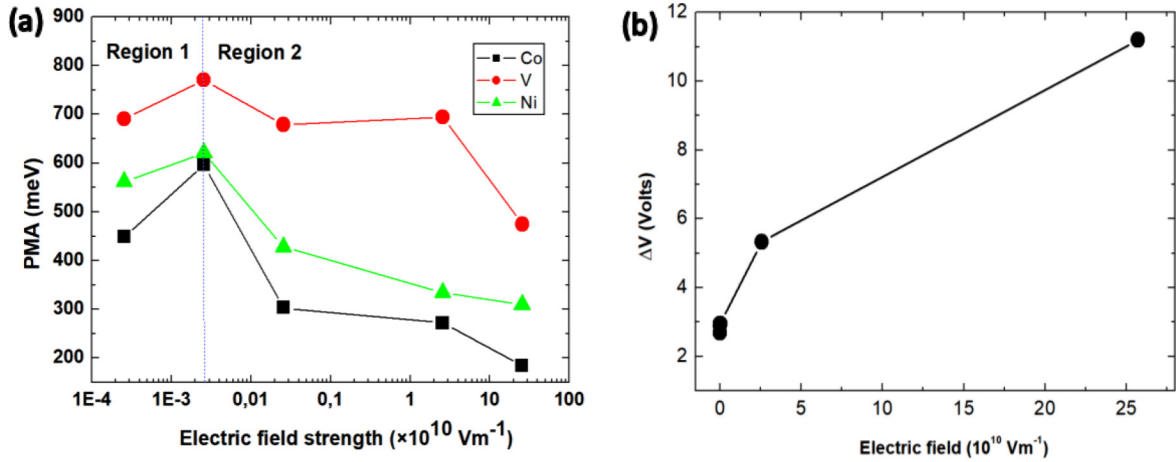


FIG. 7. Electric-field dependent PMA in Fe(110)/hBN/M stacks shown on a log-linear scale (a) and its effects on ΔV in Fe(110)/hBN/Co(111) (b). Dotted blue line shows the critical field (E_C).

obtained in Fe(110)/hBN/Ni(111) and Fe(110)/hBN/V(111), respectively. Hence, only the electric-field effects observed on the Fe(110)/hBN/Co(111) stack are discussed here due to its superior magnetization.

Electric-field dependent total energy is shown as energy offsets (Δ) relative to the zero-field configuration. It is crucial to note that the antiparallel spin configuration is energetically not suitable as a reference state for the collinear magnetization state because M_A is not guaranteed to vanish—even if M_T is zero. The change of sign in M_T is intriguing. It is physically plausible to interpret the effect of the electric field as a perturbation on the ground-state electronic structure. This approach to first-principles determination of dynamical transformations in materials properties in the presence of finite fields is widely known. For instance, description of atomic dynamics in finite electric fields yields polarization and dielectric properties of bulk MgO, in good agreement with experiments [79]. It is therefore intuitive that nontrivial transformations occur in the electronic structure due to the electric-field effect.

As the ground-state energy has no lower bound in an extended electric field [80–82], the dependence of the Fermi-surface topology on applied electric field suggests the formation of frustrated electronic order in the upper limit of region 2 (see Fig. 2). The dynamic switching of M_T is therefore ascribed to formation of an exotic phase for electron-spin

transport, in the limit of high electric fields. This interpretation is consistent with the long-lived metastable physical state that is known [81,82] to arise in response to high external electric field. Although only contributions from converged bands are included in the Landau limit, convergence tests of band energies and NMR/NQR parameters with respect to k mesh show consistent EFG and asymmetry parameters. Overall, a consistent trend emerges, wherein the electronic structure retains the flipped-spin configuration for the exotic phase at high fields.

2. Perpendicular magnetic anisotropy

Figure 7 shows the effects of electric field on PMA of pMTJs with different capping layers, and its effect on ΔV in Fe(110)/hBN/Co(111). With a zero-electric-field PMA of 394, 702, and 530 meV for Co, V, and Ni cap layers, respectively, clear separation is seen between the two regions separated by the dotted line in Fig. 7(a). This unique point marks a critical field (E_C) for all M -capped stacks and denotes the onset of an exotic transport phase. The first domain is for low electric fields (region 1), and PMAs increase (apart from $M = V$), as the applied field strength is increased. In the second region, the PMAs drop consistently with increasing applied electric field (region 2). Because PMAs drop monotonically in region 2, it is concluded that region 1 gives the upper bound in

TABLE II. Total magnetization (M_T), absolute magnetization (M_A), and magnetization energy offset (Δ) in collinear magnetization geometry of Fe(110)/hBN/Co(111) stacks at different applied electric fields. The hartree atomic unit ($1.0 \text{ a.u.} = 51.4220632 \times 10^{10} \text{ V m}^{-1}$) is used here.

Electric field (a.u.)	Electric field ($\times 10^{10} \text{ V/m}$)	Magnetization		Offset energy Δ (meV)
		M_T (μ_B/cell)	M_A (μ_B/cell)	
0	0	18.44	19.75	0
10^{-3}	0.05	18.34	19.68	-0.01
10^{-2}	0.51	18.30	19.64	-0.06
10^{-1}	5.14	-5.30	19.24	-6.25
1	51.42	-11.01	17.45	-0.01
10	514.22	-1.89	11.66	-0.06

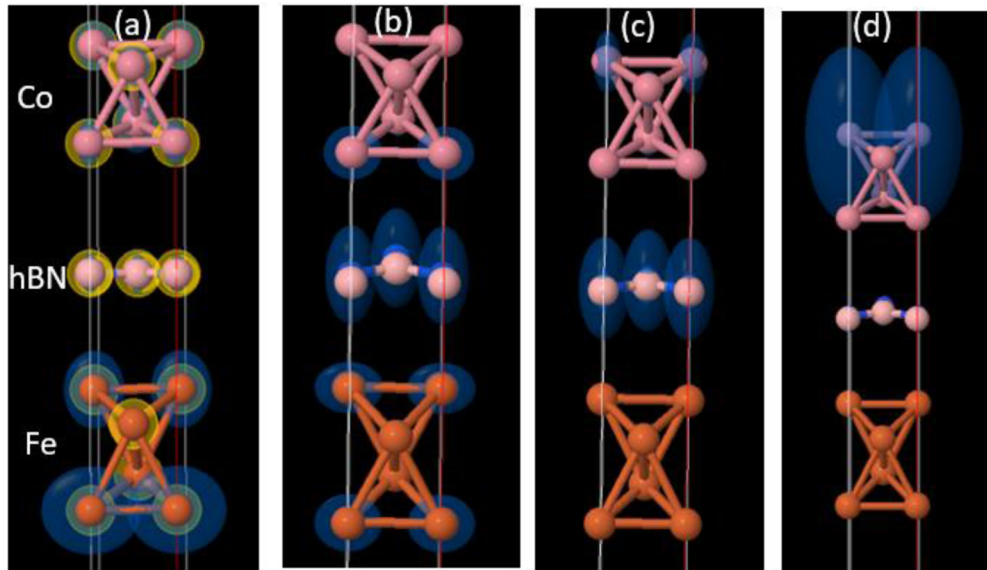


FIG. 8. Magnetic shielding (yellow) and the electric-field gradient tensors (blue) corresponding to ^{58}Co , ^{10}B , ^{14}N , and ^{57}Fe showing the local structure response to applied electric fields of magnitude: (a) 0.0, (b) 5.14, (c) 51.42, and (d) 514.22×10^{10} V/m.

VCMA. In region 1, applications of weak electric fields cause substantial increases in PMA notwithstanding the nature of the M species. In region 2, PMA reduces independently for electric-field strengths higher than the critical field, $E_c = 2.57 \times 10^7$ V/m. With $\Delta V = 2.58$ V at zero electric field, the linear relation $\Delta V \approx kE_c$ suggests that $k = 10^{-3} \text{ \AA}^{-1}$. As noted for MgO [79], constant k also relates to the step size of the finite-difference field.

Consider that the planar average charge density is peaked at about three electrons per interfacial Co layer, but drops to zero in the first Fe layer of the Fe/hBN interface in the zero-field limit [Fig. 3(a)]. As such, any loss of PMA due to the applied electric field is directly related to the response of the collinear magnetization state. Figure 7(b) shows the evolution of the electronic structure as a functional dependence of ΔV on changes in the applied electric field. Given the same critical field for all capping slabs, a linear fit to the zero-field ΔV of Fe(110)/hBN/Co(111) shows that $\Delta V \approx kE_c$, where $k = 10^{-3} \text{ \AA}^{-1}$ is constant. Perhaps this relationship holds no deeper significance since the 2.58 V is the zero-field baseline in the Fe(110)/hBN/Co(111) stack only. Although no spin-specific insight is gained in Fig. 7(b), there is an exponential increase in ΔV with increase in the applied field. The same trend also exists in the dependence of PMA on electric field in region 1.

It can be seen from Fig. 6(b) that two orientations of the net magnetization M_s are sufficient to determine the upper ($\theta = 90^\circ$) and lower ($\theta = 0^\circ$) bounds of the electric-field dependent PMA. Figure 7(a) suggests that degradation of PMA at high electric fields follows the same mechanism as the field induced loss of transverse and longitudinal magnetization in paramagnetic solids. As external electric-field dependent dynamical phenomena, the underlying processes in the microscopic responses suggest that PMA degradation and loss of magnetization independently obey the same exponential decay law as the spin-diffusion event.

One relaxation time is sufficient to characterize all the nuclei in macroscopic solids that exhibit such behavior [83]. These include systems that contain chemically distinct, and structurally inequivalent, atoms in their unit cells. In such solid-state systems, spin-diffusion events dominate, and the constituent materials experience strong dipolar interactions. Thus electric-field dependent decrease in M_A and PMA, and the induced spin flip, affect performance of pMTJs when incorporated into memory elements.

3. Coherent transfer of magnetization

Electric-field dependence of the spin transport in pMTJs is describable in terms of magnetization transfer between linked populations of spin states. This allows for the computed NQR/NMR parameters and electric-field dependence of the principal component (V_{zz}) of the EFG tensors to be compared with field and voltage conditions that induce steady-state excitations in pMTJs used in typical memory elements [84]. By only allowing internal rotation of localized spin groups [85], spin rotations about the C_3 axes of symmetry are used exclusively to determine the associated electronic order. Evolution of the spin system, in this approach, is thus restricted to the limit of coherent transfer of magnetization. Frantsuzov *et al.* [86] have argued that success of this approach to solid-state NMR relies exclusively on the relative populations of higher spin orders. For instance, the number of correlated spin states involved in a typical coherence event is noticeably small in solution-state NMR, and for which high spin order coherences are known to relax relatively quickly [87]. On the other hand, by restricting the state space in solid-state systems, very high spin orders exhibit heteronuclear decoupling in the solid state [88].

The evolution of spin transport and coherent transfer of magnetization are also considered in terms of the dipolar spin couplings and the spin texture of the Fermi-surface topology. Magnetic shielding constants (yellow spheres) and ^{58}Co , ^{10}B ,

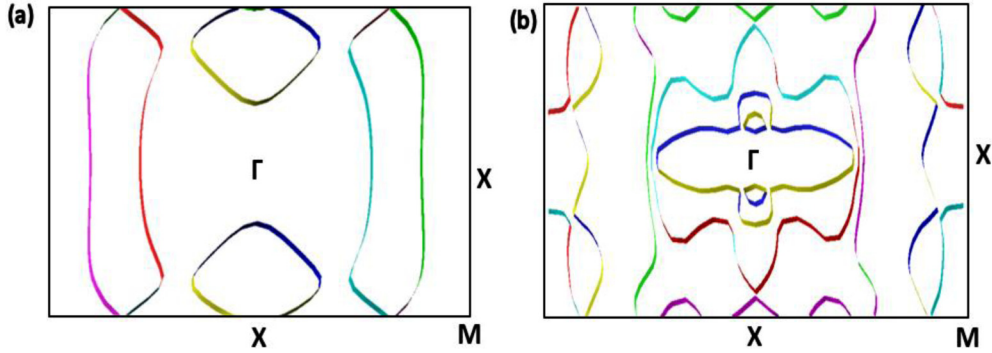


FIG. 9. Fermi-surface topology in the upper limit of the Coulomb regime for parallel (a) and antiparallel (b) alignments of the spin magnetic moment.

^{14}N , and ^{57}Fe EFGs (blue ellipsoids) are shown in Fig. 8. At zero electric field, the EFG tensor is symmetric and the magnetic shielding tensor is antisymmetric [Fig. 8(a)]. The size and orientations of EFG ellipsoids localized on constituent atoms respond differently to the electric field. Local atomic responses are describable in terms of the isotropy, anisotropy, and asymmetry of the ellipsoids. The EFG tensor of the top (or bottom) Fe-layer atoms exhibits prolate (or oblate) symmetry [Fig. 8(a)] while those of the two middle planes of the Fe layer vanish independently. On B and N atoms, EFGs are small albeit nonzero. The prolate symmetry displays weak sensitivity to the layer index of Co. Figures 8(b) and 8(d) show independently vanishing magnetic shielding constants at all nonzero external electric fields. The B and N atoms acquire finite EFGs independent of the two-order-of-magnitude increase in applied field from 5.14×10^{10} to 5.14×10^{12} V/m. In the same field range, it reduces to zero on both Fe and Co species. Only the topmost Co-layer atoms acquire nonzero EFGs at 5.142×10^{11} V/m [Figs. 8(c) and 8(d)], and this increases significantly at 5.14×10^{12} V/m. Similar trends [Fig. 8(d)] suggest that the Co layer dominates local responses. Though EFG localization on the topmost layer Co at 10 a.u. is as large as 1 a.u., it vanishes completely in the second, third, and fourth atomic planes.

Figure 9 shows the Fermi surfaces in the upper limit of the Coulomb regime. A comparison of Figs. 9(a) and 9(b) with Figs. 4(b) and 4(d) reveals key changes in the Fermi-surface topology as the applied electric-field intensity increases. The evolution of the electronic structure reveals that electron and hole states, though symmetrically distributed at the Fermi

level, result in a frustrated electronic order since all the atoms at the interfaces do not respond in the same way. In particular, the distribution of electron and hole states along nodal rings on the $(k_x, k_y \equiv 0, 0)$ mirror plane of the Brillouin zone is symmetrical. The absence of broken chiral symmetry in the topology of this exotic electronic phase shows the coherence of its spin state. Far fewer node lines and Fermi arcs become available for transport relative to zero field. Importantly, the spacing between the few surviving Fermi arcs increases considerably in both parallel and antiparallel spin alignments. In the lower (or upper) limit of the Coulomb regime, the number of the electron and hole transport channels increases (or reduces). Increased electric-field intensity also results in a significant change in the shape, size, and distribution of carrier pockets [Figs. 9(a) and 9(b)] relative to the zero-field case [Figs. 4(b) and 4(d)].

4. Response of the spin current

Table III shows the effects of the electric and magnetic field on the spin transmission coefficients at the Fermi level $T(E_F)$. Parallel spin configuration (relative to the alignment of the external magnetic field) yields larger changes in the up-spin $T(E_F)$ for any order-of-magnitude change in the applied electric field. Conversely, the spin-down $T(E_F)$ yields negligibly small spectral changes, suggesting that transmission of spin-down current is robust to perturbations. Two opposing trends are seen in the antiparallel spin configuration. Spin-up (or spin-down) transmission is comparatively more robust to electric-field changes in the Coulomb (or intermediate) regime. The applied electric field has other nontrivial effects

TABLE III. Electric- and magnetic-field effects on spin transmission coefficients at the Fermi level.

Perturbation	Magnetic field alignment					
	Intensity		Parallel		Antiparallel	
	(a.u.)	(10^{10} V/m)	Up	Down	Up	Down
Zero field	0	0	0.19	0.16	0.61	0.01
Coulomb	10^{-3}	0.05	0.29	0.18	0.66	0.31
	10^{-2}	0.51	3.72	0.62	3.94	1.04
Intermediate	10^{-1}	5.14	5.85	1.86	1.59	3.13
	1	51.42	3.72	0.81	0.33	3.13
Landau	10	514.22	0.20	0.14	0.03	0.71

on the spin transmission spectrum. First, $T(E_F)$ reduces by a factor of 5.73 (and 1.96) for up-spin (and down-spin) carriers when the electric field is increased from 0.1 to 1.0 Hartree a.u. in the parallel spin orientation. Ramping up the electric field within the Coulomb regime results in correspondingly high $T(E_F)$. Crucially, this observation is not dependent on magnetic field alignment of spin to either parallel or antiparallel orientation. Second, the down-spin $T(E_F)$ is dominant in the antiparallel spin configuration whenever the applied electric field exceeds the Coulomb limit.

To obtain deeper insights to the spin-flipped configuration, trends in the spin transmission spectra (Fig. 5) are compared with results of inelastic electron tunneling spectroscopy (IETS) on the somewhat similar graphite/CrI₃/graphite [78] and graphite/boron nitride/graphite [89] van der Waals heterostructure stacks. First, the zero-bias spin conductance peaks are unique signatures of the efficient spin inversion and filtering in Fe(110)/hBN/Co(111). Recently, Asshoff *et al.* [90] showed that resonant tunneling through single defects in the related Co/hBN/NiFe heterostructure enhances the magnetoresistance. Second, the calculated electric-field dependent spin transmission coefficients $T(E_F)$ exhibit two opposing trends. Spin-up (or spin-down) transmission of the antiparallel spin configuration is robust to electric-field changes in the Coulomb (or intermediate) regime unlike the parallel spin configuration. These trends typify the spin-flip scattering first observed by Guinea in tunnel junctions [91]. Third, inelastic magnon-assisted tunneling spectroscopy of similar multilayers that contain CrBr₃ in the tunnel barrier [92] suggests that the sign change of M_T is attributable to the formation of a spin-sensitive transport phase due to magnon emission at low temperature.

At $T \neq 0$ K, by contrast, the observed sign change in M_T represents the induced spin-flip phase detected in planar metal-hexagonal boron nitride-graphene junctions at high energy [93]. In our case, this high-energy phase is only observed in the Fe(110)/hBN/Co(111) multilayer when the spin system is subjected to high electric field in the presence of the external magnetic field. Klein *et al.* [78] interprets the delocalized spin flip of a *large* magnetic moment $\sim 2 \mu_B$ (i.e., $|S_z| = 1$) antiparallel to the external magnetic field as a single magnon process that occurs within the CrI₃ tunnel barrier. The IETS data show that the magnon peaks are blueshifted at 0.12 meV/T by the associated Zeeman effect. Since the external

backgate used in [94,95] has analogous effects to the applied electric field, local structure responses will vanish when the perturbing-field intensity is lower than the upper bound of the field limit. Hence, the creation of spin-sensitive dynamical signatures through the effect of electric field on carriers [95] and quasiparticles [96] using ionic gating, gate voltage, or an axial electric field offers scientifically interesting and technologically important avenues to achieve precise control of tunneling spin currents.

IV. CONCLUSIONS

In conclusion, first-principles calculations have been performed to gain insights into the dynamical effects created by external axial fields in the Fe(110)/hBN-based pMTJs. It is found that even at moderate intensities the applied electric field can flip the direction of the resultant magnetization vector relative to the alignment of the magnetic field. The associated dynamical effects are modulated by substantial anisotropies in the Fermi-level topology. Importantly, magnetic properties such as magnetization density, perpendicular magnetic anisotropy, and spin transmission coefficients of pMTJs are found to exhibit anomalous dependence on the external electric field. Within the linear response regime, the spin-flip disorder is observed in magnetic states at high electric fields. Nontrivial warping of electron-hole pockets in the first Brillouin zone has been used to establish the existence of an exotic transport phase for spin carriers. From the sensitivity of the Fermi-surface topology to the field-driven disorder, it is concluded that the electronic response is field tunable. Since the Fermi surface in the component materials of a stack undergoes independent transitions when time-reversal symmetry is broken, insights gained herein offer pathways for the spectroscopic characterization of the local responses in pMTJs especially when subjected to large axial fields in spin transport, and optoelectronic, devices.

ACKNOWLEDGMENTS

This work was funded by the National Research Foundation of South Africa (Grant No. 15056). The author thanks the Center for High Performance Computing for computing time on the Lengau supercomputer under Research Program No. MATS0941.

-
- [1] J.-H. Kim, J.-B. Lee, G.-G. An, S.-M. Yang, W.-S. Chung, H.-S. Park, and J.-P. Hong, *Sci. Rep.* **5**, 16903 (2015).
 - [2] M. Gurram, S. Omar, and B. J. van Wees, *Nat. Commun.* **8**, 248 (2017).
 - [3] M. Piquemal-Banci, R. Galceran, S. Caneva, M.-B. Martin, R. S. Weatherup, P. R. Kidambi, K. Bouzeshouane, S. Xavier, A. Anane, F. Petroff, A. Fert, J. Robertson, S. Hofmann, B. Dlubak, and P. Seneor, *Appl. Phys. Lett.* **108**, 102404 (2016).
 - [4] M. Piquemal-Banci, R. Galceran, M.-B. Martin, F. Godel, A. Anane, F. Petroff, B. Dlubak, and P. Seneor, *J. Phys. D* **50**, 203002 (2017).
 - [5] A. M. Ukpogon, *J. Phys. D* **51**, 095302 (2018).
 - [6] P. Willke, T. Kotzott, T. Pruschke, and M. Wenderoth, *Nat. Commun.* **8**, 15283 (2017).
 - [7] P. Kumar, V. Sharma, F. A. Reboredo, L.-M. Yang, and R. Pushpa, *Sci. Rep.* **6**, 31841 (2016).
 - [8] I. G. Rau, S. Baumann, S. Rusponi, F. Donati, S. Stepanow, L. Gragnaniello, J. Dreiser, C. Piamonteze, F. Nolting, and S. Gangopadhyay *et al.*, *Science* **344**, 988 (2014).
 - [9] R. Skomski, *J. Phys.: Condens. Matter* **15**, R841 (2003).
 - [10] W. Yan, O. Txoperena, R. Llopis, H. Dery, L. E. Hueso, and F. Casanova, *Nat. Commun.* **7**, 13372 (2016).
 - [11] A. M. Ukpogon, *J. Phys.: Condens. Matter* **29**, 285302 (2017).

- [12] S. Bruzzone, D. Logoteta, G. Fiori, and G. Iannaccone, *Sci. Rep.* **5**, 4519 (2015).
- [13] K. Zollner, M. Gmitra, T. Frank, and J. Fabian, *Phys. Rev. B* **94**, 155441 (2016).
- [14] A. H. Larsen, J. J. Mortensen, J. Blomqvist, I. E. Castelli, R. Christensen, M. Dułak, J. Friis, M. N. Groves, B. Hammer, C. Hargus, E. D. Hermes, P. C. Jennings, P. B. Jensen, J. Kermode, J. R. Kitchin, E. L. Kolsbjerg, J. Kubal, K. Kaasbjerg, S. Lysgaard, J. B. Maronsson, T. Maxson, T. Olsen, L. Pastewka, A. Peterson, C. Rostgaard, J. Schiøtz, O. Schütt, M. Strange, K. S. Thygesen, T. Vegge, L. Vilhelmsen, M. Walter, Z. Zeng, and K. Wedel Jacobsen, *J. Phys.: Condens. Matter* **29**, 273002 (2017).
- [15] T. Thonhauser, S. Zuluaga, C. A. Arter, K. Berland, E. Schröder, and P. Hyldgaard, *Phys. Rev. Lett.* **115**, 136402 (2015).
- [16] P. Giannozzi, S. Baroni, N. Bonini, M. Calandra, R. Car, C. Cavazzoni, D. Ceresoli, G. L. Chiarotti, M. Cococcioni, I. Dabo, A. Dal Corso, S. de Gironcoli, S. Fabris, G. Fratesi, R. Gebauer, U. Gerstmann, C. Gougoussis, A. Kokalj, M. Lazzeri, L. Martin-Samos, N. Marzari, F. Mauri, R. Mazzarello, S. Paolini, A. Pasquarello, L. Paulatto, C. Sbraccia, S. Scandolo, G. Sclauzero, A. P. Seitsonen, A. Smogunov, P. Umari, and R. M. Wentzcovitch, *J. Phys. Condens. Matter* **21**, 395502 (2009).
- [17] M. Dion, H. Rydberg, E. Schröder, D. C. Langreth, and B. I. Lundqvist, *Phys. Rev. Lett.* **92**, 246401 (2004).
- [18] K. Lee, E. D. Murray, L. Kong, B. I. Lundqvist, and D. C. Langreth, *Phys. Rev. B* **82**, 081101(R) (2010).
- [19] E. D. Murray, K. Lee, and D. C. Langreth, *J. Chem. Theory Comput.* **5**, 2754 (2009).
- [20] J. P. Perdew and Y. Wang, *Phys. Rev. B* **33**, 8800 (1986).
- [21] K. Berland and P. Hyldgaard, *Phys. Rev. B* **89**, 035412 (2014).
- [22] H. J. Monkhorst and J. D. Pack, *Phys. Rev. B* **13**, 5188 (1976).
- [23] N. Marzari, D. Vanderbilt, A. De Vita, and M. C. Payne, *Phys. Rev. Lett.* **82**, 3296 (1999).
- [24] G. Kresse and D. Joubert, *Phys. Rev. B* **59**, 1758 (1999).
- [25] S. Datta, *Electronic Transport in Mesoscopic Systems* (Cambridge University, Cambridge, England, 1999).
- [26] D. Li, C. Barreateau, and A. Smogunov, *Phys. Rev. B* **93**, 144405 (2016).
- [27] M. Weinert, R. E. Watson, and J. W. Davenport, *Phys. Rev. B* **32**, 2115 (1985).
- [28] G. H. O. Daalderop, P. J. Kelly, and M. F. H. Schuurmans, *Phys. Rev. B* **41**, 11919 (1990).
- [29] J. Zhang, P. V. Lukashev, S. S. Jaswal, and E. Y. Tsybmal, *Phys. Rev. B* **96**, 014435 (2017).
- [30] M. Otani and O. Sugino, *Phys. Rev. B* **73**, 115407 (2006).
- [31] Y.-P. Wang and H.-P. Cheng, *Phys. Rev. B* **91**, 245307 (2015).
- [32] T. Sohler, M. Calandra, and F. Mauri, *Phys. Rev. B* **96**, 075448 (2017).
- [33] A. Dal Corso, *Phys. Rev. B* **82**, 075116 (2010).
- [34] A. Baldereschi, S. Baroni, and R. Resta, *Phys. Rev. Lett.* **61**, 734 (1988).
- [35] G. Giovannetti, P. A. Khomyakov, G. Brocks, V. M. Karpan, J. van den Brink, and P. J. Kelly, *Phys. Rev. Lett.* **101**, 026803 (2008).
- [36] A. B. Preobrajenski, S. A. Krasnikov, A. S. Vinogradov, M. L. Ng, T. Käåmbre, A. A. Cafolla, and N. Mårtensson, *Phys. Rev. B* **77**, 085421 (2008).
- [37] L. H. Li, Y. Chen, G. Behan, H. Z. Zhang, M. Petracic, and A. M. Glushenkov, *J. Mater. Chem.* **21**, 11862 (2011).
- [38] V. L. Solozhenko, G. Will, and F. Elf, *Solid State Commun.* **96**, 1 (1995).
- [39] M. Topsakal, E. Aktürk, and S. Ciraci, *Phys. Rev. B* **79**, 115442 (2009).
- [40] L.-C. Yin, H.-M. Cheng, and R. Saito, *Phys. Rev. B* **81**, 153407 (2010).
- [41] B. Huang and H. Lee, *Phys. Rev. B* **86**, 245406 (2012).
- [42] See Supplemental Material at <http://link.aps.org/supplemental/10.1103/PhysRevB.100.035424> for more details of the total energy, and adhesion energy convergence tests, which verify that the slab models result in stable stacks of coupled multilayers.
- [43] R. W. Lynch and H. G. Drickamer, *J. Chem. Phys.* **44**, 181 (1966).
- [44] J. D. H. Donnay, W. P. Mason, and E. A. Wood, in *American Institute of Physics Handbook*, 3rd ed., edited by D. M. Gray (McGraw-Hill, New York, 1972), pp. 9–5.
- [45] C. Yelgel, *J. Appl. Phys.* **119**, 065307 (2016).
- [46] S. Nakanishi and T. Horiguchi, *Jpn. J. Appl. Phys.* **20**, L214 (1981).
- [47] T. Gourieux, S. Fréchar, F. Dulot, J. Eugène, B. Kierren, and D. Malterre, *Phys. Rev. B* **62**, 7502 (2000).
- [48] *CRC Handbook of Chemistry and Physics*, 92nd ed., edited by W. M. Haynes (CRC, Boca Raton, FL, 2012).
- [49] P. Rochana and K. Lee, and J. Wilcox, *J. Phys. Chem. C* **118**, 4238 (2014).
- [50] J.-Y. Lee, M. P. J. Punkkinen, S. Schönecker, Z. Nabi, K. Kádas, V. Zólyomi, Y. M. Koo, Q.-M. Hu, R. Ahuja, B. Johansson, J. Kollár, L. Vitos, and S. K. Kwon, *Surf. Sci.* **674**, 51 (2018).
- [51] M. J. S. Spencer, A. Hung, I. K. Snook, and I. Yarovsky, *Surf. Sci.* **513**, 389 (2002).
- [52] R. Kohlhaas, P. Donner, and N. Schmitz-Pranghe, *Z. Angew. Phys.* **23**, 245 (1967).
- [53] P. Błoński and A. Kiejna, *Vacuum* **74**, 179 (2004).
- [54] M. S. Si, J. Y. Li, H. G. Shi, X. N. Niu, and D. S. Xue, *Europhys. Lett.* **86**, 46002 (2009).
- [55] S. Azevedo, J. R. Kaschny, C. M. C. de Castilho, and M. F. de Brito, *Eur. Phys. J. B.* **67**, 507 (2009).
- [56] Y. Kubota, K. Watanabe, O. Tsuda, and T. Taniguchi, *Science* **317**, 932 (2007).
- [57] K. Ba, W. Jiang, J. Cheng, J. Bao, N. Xuan, Y. Sun, B. Liu, A. Xie, S. Wu, and Z. Sun, *Sci. Rep.* **7**, 45584 (2017).
- [58] A. Dannenberg, M. E. Gruner, A. Hucht, and P. Entel, *Phys. Rev. B* **80**, 245438 (2009).
- [59] S. Schönecker, X. Li, B. Johansson, S. K. Kwon, and L. Vitos, *Sci. Rep.* **5**, 14860 (2015).
- [60] G. Autès, C. Barreateau, D. Spanjaard, and M.-C. Desjonqueres, *J. Phys.: Condens. Matter* **18**, 6785 (2006).
- [61] J. Dauber, A. A. Sagade, M. Oellers, K. Watanabe, T. Taniguchi, D. Neumaier, and C. Stampfer, *Appl. Phys. Lett.* **106**, 193501 (2015).
- [62] M. V. Kamalakar, C. Groenveld, A. Dankert, and S. P. Dash, *Nat. Commun.* **6**, 6766 (2015).
- [63] A. Dankert, M. V. Kamalakar, A. Wajid, R. S. Patel, and S. P. Dash, *Nano Res.* **8**, 1357 (2015).
- [64] P. U. Asshoff, J. L. Sambricio, A. Mishchenko, A. P. Rooney, E. W. Hill, S. J. Haigh, A. K. Geim, V. I. Fal'ko, I. J. Vera-Marun, and I. V. Grigorieva, *2D Mater.* **4**, 031004 (2016).

- [65] M. V. Kamalakar, A. Dankert, P. J. Kelly, and S. P. Dash, *Sci. Rep.* **6**, 21168 (2016).
- [66] M. Z. Iqbal, M. W. Iqbal, S. Siddique, M. F. Khan, and S. M. Ramay, *Sci. Rep.* **6**, 21038 (2016).
- [67] M. V. Kamalakar, A. Dankert, J. Bergsten, T. Ive, and S. P. Dash, *Sci. Rep.* **4**, 6146 (2014).
- [68] M. Z. Iqbal, M. W. Iqbal, J. H. Lee, Y. S. Kim, S.-H. Chun, and J. Eom, *Nano Res.* **6**, 373 (2013).
- [69] M. Z. Iqbal, S. Siddique, G. Hussain, and M. W. Iqbal, *J. Mater. Chem. C* **4**, 8711 (2016).
- [70] P. J. Zomer, S. P. Dash, N. Tombros, and B. J. van Wees, *Appl. Phys. Lett.* **99**, 232104 (2011).
- [71] B. Dublak, M.-B. Martin, C. Deranlot, B. Servet, S. Xavier, R. Mattana, M. Sprinkle, C. Berger, W. A. De Heer, F. Petroff, A. Anane, P. Seneor, and A. Fert, *Nat. Phys.* **8**, 557 (2012).
- [72] M. Piquemal-Banci, R. Galceran, F. Godel, S. Caneva, M.-B. Martin, R. S. Weatherup, P. R. Kidambi, K. Bouzehouane, S. Xavier, A. Anane, F. Petroff, A. Fert, S. M.-M. Dubois, J.-C. Charlier, J. Robertson, S. Hofmann, B. Dlubak, and P. Seneor, *ACS Nano* **12**, 4712 (2018).
- [73] H. Weng, Y. Liang, Q. Xu, R. Yu, Z. Fang, X. Dai, and Y. Kawazoe, *Phys. Rev. B* **92**, 045108 (2015).
- [74] Y. Du, F. Tang, D. Wang, L. Sheng, E.-j. Kan, C.-G. Duan, S. Y. Savrasov, and X. Wan, *Quantum Materials* **2**, 3 (2018).
- [75] A. Topp, J. M. Lippmann, A. Varykhalov, V. Duppel, B. V. Lotsch, C. R. Ast, and L. M. Schoop, *New J. Phys.* **18**, 125014 (2016).
- [76] T. Nozaki, N. Tezuka, and K. Inomata, *Phys. Rev. Lett.* **96**, 027208 (2006).
- [77] D. Li, Y. J. Dappe, and A. Smogunov, *Phys. Rev. B* **93**, 201403(R) (2016).
- [78] D. R. Klein, D. MacNeill, J. L. Lado, D. Soriano, E. Navarro-Moratalla, K. Watanabe, T. Taniguchi, S. Manni, P. Canfield, J. Fernández-Rossier, and P. Jarillo-Herrero, *Science* **360**, 1218 (2018).
- [79] P. Umari and A. Pasquarello, *Phys. Rev. Lett.* **89**, 157602 (2002).
- [80] G. H. Wannier, *Phys. Rev.* **117**, 432 (1960).
- [81] G. Nenciu, *Rev. Mod. Phys.* **63**, 91 (1991).
- [82] R. W. Nunes and D. Vanderbilt, *Phys. Rev. Lett.* **73**, 712 (1994).
- [83] V. I. Bakhmutov, *NMR Spectroscopy in Liquids and Solids* (CRC, Boca Raton, FL, 2015).
- [84] A. Atitoaie, I. Firastrau, L. D. Buda-Prejbeanu, U. Ebels, and M. Volmer, *J. Appl. Phys.* **124**, 093902 (2018).
- [85] R. Goc, *Comput. Phys. Commun.* **162**, 102 (2004).
- [86] I. Frantsuzov, M. Ernst, S. P. Brown, and P. Hodgkinson, *Solid State Nucl. Magn. Reson.* **70**, 28 (2015).
- [87] A. Karabanov, I. Kuprov, G. T. P. Charnock, A. van der Drift, L. J. Edwards, and W. Kockenberger, *J. Chem. Phys.* **135**, 084106 (2011).
- [88] V. S. Mithu, S. Paul, N. D. Kurur, and P. K. Madhu, *J. Magn. Reson.* **209**, 359 (2011).
- [89] S. Jung, M. Park, J. Park, T.-Y. Jeong, H.-J. Kim, K. Watanabe, T. Taniguchi, D. H. Ha, C. Hwang, and Y.-S. Kim, *Sci. Rep.* **5**, 16642 (2015).
- [90] P. U. Ashhoff, J. Z. Sambricio, S. Slizovskiy, A. P. Rooney, T. Taniguchi, K. Watanabe, S. J. Haigh, V. Fal'ko, I. V. Grigorieva, and I. J. Vera-Marun, *Nano Lett.* **18**, 6954 (2018).
- [91] F. Guinea, *Phys. Rev. B* **58**, 9212 (1998).
- [92] D. Ghazaryan, M. T. Greenaway, Z. Wang, V. H. Guaroichico-Moreira, I. J. Vera-Marun, J. Yin, Y. Liao, S. V. Morozov, O. Kristanovski, A. I. Lichtenstein, M. I. Katsnelson, F. Withers, A. Mishchenko, L. Eaves, A. K. Geim, K. S. Novoselov, and A. Misra, *Nat. Electronics* **1**, 344 (2018).
- [93] U. Chandni, K. Watanabe, T. Taniguchi, and J. P. Eisenstein, *Nano Lett.* **16**, 7982 (2016).
- [94] D. D. Felice and Y. J. Dappe, *Nanotechnology* **29**, 505708 (2018).
- [95] N. Djavid, G. Yin, Y. Barlas, and R. K. Lake, *Appl. Phys. Lett.* **113**, 012601 (2018).
- [96] P. Dufek, P. Blaha, and K. Schwarz, *Phys. Rev. Lett.* **75**, 3545 (1995).